Journal of
Renewable Energy Research and Applications (RERA)
Vol. 7, No 1, 2026, 49- 62 DOI: 10.22044/rera.2025.16795.1464

Experimental assessment of aluminum heat sink geometries on temperature mitigation and power output in PV panels under natural convection

R. Ahmadi and A. Sarreshtehdari*

Mechanical Engineering Department, Shahrood University of Technology, Shahrood, Iran.

Received Date 12 September 2025; Revised Date 19 November 2025; Accepted Date 09 December 2025
**Corresponding author: sarreshtehdari@shahroodut.ac.ir (A. Sarreshtehdari)*

Abstract

Photovoltaic (PV) panels experience efficiency losses due to elevated operating temperatures, particularly in high-insolation regions where overheating reduces power output and module lifespan. This issue is exacerbated in arid climates such as Iran, where abundant solar resources coincide with extreme heat, emphasizing the need for cost-effective passive cooling. Prior research focuses on active cooling or wind-assisted methods, overlooking natural convection under stagnant conditions and the use of commercially available materials. To address these gaps, this study evaluates the thermal and electrical benefits of repurposing industrial aluminum profiles as heat sinks for PV panels, offering a sustainable solution using off-the-shelf components without custom fabrication. Experiments employed a controlled laboratory setup with a monocrystalline PV panel under 1000 W/m² irradiation and zero wind speed. Three aluminum profiles, varying in mass and geometry, were attached to the panel's rear and compared to an uncooled reference. Measurements included time-dependent surface temperatures, power outputs, thermal imaging, and uncertainty analysis for reliability. Findings indicated time-dependent effects: during the initial heating phase (0–30 minutes), heat sinks reduced temperatures (up to 2.56°C for the heaviest model) and increased power (up to 1.65%). In the stabilization phase (30–60 minutes), temperatures exceeded the reference (by 0.25–1.57°C), causing slight power drops (0.67–1.24%). Heavier profiles delayed stabilization but risked hot air entrapment. These time-dependent effects underscore the potential of aluminum heat sinks for modest PV performance improvements under zero-wind conditions, albeit with trade-offs in long-term stability. These findings emphasize the importance of geometry selection for enhancing natural convection efficiency in stagnant-air PV applications.

Keywords: *Passive Cooling, Photovoltaic (PV) Cooling, Aluminum Heat Sink, Temperature Reduction, Natural Convection.*

1. Introduction

Photovoltaic (PV) systems have emerged as a cornerstone of renewable energy strategies worldwide, converting solar radiation into electricity with increasing efficiency. However, one persistent issue in their operation is thermal degradation caused by elevated temperatures, which can significantly impair power output and longevity. This study focuses on passive cooling techniques, specifically the application of aluminum heat sink geometries to mitigate temperature rises in PV panels under controlled irradiation conditions. By attaching heat sinks to the rear of PV modules, heat can be dissipated through natural convection, potentially enhancing electrical performance without the need for energy-intensive active systems. The significance of this topic lies in its alignment with global efforts to optimize solar energy harvesting, particularly in regions with high solar insolation where overheating is a common challenge [1–3].

Recent advancements in thermal management have highlighted how material properties and geometric designs influence heat transfer, offering practical solutions for improving PV efficiency [2–4]. In essence, exploring heat sink configurations not only addresses immediate performance losses but also contributes to the broader goal of sustainable energy production by making PV technology more resilient to environmental stressors.

The growing relevance of PV cooling stems from the well-documented negative temperature coefficient of silicon-based solar cells, where efficiency drops by approximately 0.4–0.5% per degree Celsius above 25°C [5, 6]. This phenomenon becomes particularly pronounced in hot climates, leading to substantial energy yield reductions over time. Factors such as rising global temperatures and the expansion of solar installations in arid areas have amplified the need for effective cooling methods [7–9]. For instance, studies have demonstrated that passive cooling can extend module lifespan and boost annual energy output by maintaining optimal operating temperatures [8–10]. Moreover, the economic implications are compelling; as PV deployment scales up, even modest improvements in efficiency translate into significant cost savings and reduced carbon footprints [11, 12]. In the context of emerging markets like Iran, where abundant sunlight coexists with extreme heat, locally sourced materials such as aluminum profiles present a cost-effective avenue for innovation [13, 14]. This study is motivated by these dynamics, aiming to evaluate how specific heat sink designs can counteract thermal inefficiencies, thereby supporting the transition to more reliable renewable energy systems [15, 16].

Shifting from broad motivations, it is worth considering the practical drivers. Advances in manufacturing have made aluminum heat sinks readily available and adaptable, yet their integration into PV systems requires empirical validation to ensure real-world applicability [17, 18]. The rationale extends beyond technical feasibility to environmental benefits, as enhanced PV performance reduces reliance on fossil fuels [19, 20]. Ultimately, investigating these elements underscores the urgency of refining cooling strategies to meet escalating energy demands sustainably.

Despite progress, several challenges persist in PV thermal management. High ambient temperatures often lead to uneven heat distribution across panels, exacerbating hot spots and accelerating degradation [21, 22]. Passive cooling via heat sinks faces limitations under low-wind conditions, where natural convection may be insufficient, resulting in suboptimal heat dissipation [23, 24]. Additionally, geometric variations in heat sinks—such as fin density and surface area—can either enhance or hinder airflow, sometimes trapping heat rather than expelling it [4–6]. These issues are compounded by material costs and the need for designs that balance weight, thermal conductivity, and ease of installation.

On the opportunity side, recent research points to promising pathways. Optimized heat sink geometries have shown potential to reduce panel temperatures by several degrees, directly correlating with power gains [2, 5]. For example, integrating phase-change materials or hybrid approaches with aluminum profiles could amplify cooling effects [1, 3]. Opportunities also arise from computational modeling, which allows for predictive analysis of heat transfer dynamics before physical prototyping [7, 9]. In resource-constrained settings, leveraging industrial aluminum waste or locally produced profiles opens doors to scalable, eco-friendly solutions [13, 15]. Furthermore, as PV systems evolve toward building-integrated designs, heat sinks offer dual benefits: cooling the panels while potentially recovering waste heat for other uses [16, 18]. These prospects highlight how addressing current hurdles through targeted experimentation can unlock substantial improvements in system efficiency and durability [19, 22].

While existing literature provides valuable insights into PV cooling, notable gaps remain that this study seeks to address. Many prior investigations focus on forced convection or active cooling, often overlooking the nuances of natural convection in wind-free environments, which better simulate real-world stagnation scenarios [8, 11]. For instance, studies have examined heat sink performance but frequently limit analyses to short durations or ignore time-dependent effects, such as initial heating versus stabilization phases [14, 17]. There is also a scarcity of comparative evaluations using commercially available aluminum profiles, particularly in terms of mass, contact area, and fin shape impacts on both thermal and electrical outcomes [20, 23]. Uncertainty analyses are inconsistently applied, leading to questions about result reproducibility [24]. Additionally, much of the research emphasizes theoretical modeling over empirical data from controlled laboratory setups, leaving uncertainties in practical implementation [1, 4]. These limitations justify further exploration, as they hinder the development of tailored solutions for diverse climatic conditions [5, 6]. By filling these voids, this work aims to provide a more comprehensive understanding of passive cooling dynamics.

The primary objective of this research is to experimentally assess the influence of three distinct aluminum heat sink geometries on temperature reduction and power output in a monocrystalline PV panel under controlled irradiation of approximately 1000 W/m² and zero wind speed. Through detailed measurements and uncertainty evaluations, the study seeks to quantify time-dependent performance variations and offer insights into optimal design parameters for natural convection cooling. Previous works [1–5, 17, 21] have explored both active and passive cooling approaches, yet many relied on forced convection or customized fin geometries, overlooking commercial profiles and stagnant air conditions. Moreover, the transient heating phase has rarely been analyzed, leading to an incomplete understanding of time-dependent thermal behavior. Hence, this study bridges these gaps by experimentally investigating industrial, low-cost aluminum profiles under wind-free conditions, thereby extending the knowledge on natural convection cooling in realistic stationary scenarios.

The main novelties of the present study are:

(i) utilization of readily available industrial aluminum profiles as heat sinks—no custom fabrication required.

(ii) controlled laboratory tests under zero wind speed, isolating natural convection effects.

(iii) time-dependent analysis distinguishing short-term thermal buffering from steady-state behavior.

(iv) incorporation of detailed uncertainty analysis to establish repeatability and reliability.

2. Materials and methods

This section describes the experimental methodology for evaluating the effect of different aluminum heat sink geometries on the temperature drop and power output of photovoltaic (PV) panels under natural convection only and controlled irradiation, simulating a worst-case scenario with zero wind speed. The approach emphasizes repeatability, accuracy, and cost-effectiveness, and uses a laboratory setup to compare heat sink configurations in this initial evaluation. The experiments focused on investigating the effects of heat sink geometry (such as fin shape, mass, and contact area) on thermal dissipation and electrical performance. All procedures were performed according to standard protocols in solar energy research, and measurements were taken in a controlled indoor environment to eliminate variables such as wind or changing environmental conditions.

2.1. Experimental setup

The setup was designed to simulate solar irradiation while monitoring PV panel responses to different heat sink geometries. As shown in figure 1(a) (schematic diagram) and figure 1(b) (photograph of the experimental setup), they included core components:

- PV Panel: In this experimental work, a monocrystalline silicon PV module (model NN-M36-20W, Ma Solar, China) with 36 cells and total dimensions of 330 × 400 mm was used. Table 1 summarizes the specifications. The panel was mounted horizontally on an iron-aluminum frame using cotton straps. The aluminum panel frame was removed so that the panel could be considered as part of a larger panel.
- Solar Simulator: Three parallel 400 W metal halide lamps (model HQI-T400-D, OSRAM) were placed in an MDF frame with aluminum reflectors to create uniform light distribution. The distance between the lamps and the panel was fixed, and ventilation ducts were created above each lamp to prevent heat retention caused by waste heat from the lamps. Irradiance was maintained at approximately 1000 W/m² ±3% across the panel surface, measured using a digital pyranometer (model MIC-98206, MIC) positioned at the center of the panel. The sensor detects total solar radiation, with readings taken at the start of each experiment to ensure uniformity.
- Heat sinks: Three different industrial aluminum profiles were evaluated for their thermal performance, selected based on commercial availability in Iran, low cost (≈4 USD/kg), and variability in design parameters. The geometric, price, and physical specifications of the aluminum heat sink models are presented in table 2. The schematic and actual shapes of the profiles are shown in figure 2(a) and figure 2(b), respectively. Each heat sink was affixed to the PV panel's rear surface using a thin layer of silicone adhesive to improve heat transfer between the panel and the heat sink. Heat sinks were chosen from available profiles in the Iranian market to compare the effects of their mass, surface area, and geometries on heat dissipation via natural convection and radiation. The comparative scenarios included a reference model without a heat sink, along with each individual heat sink model.

Conducted in Karaj home lab (3x4.5x2.8 m sealed room, no ventilation/windows; 25-27°C, RH 35-40% per meteo data). Reference: 3 runs (consistent <1% variation); cooled models: single-run baseline.

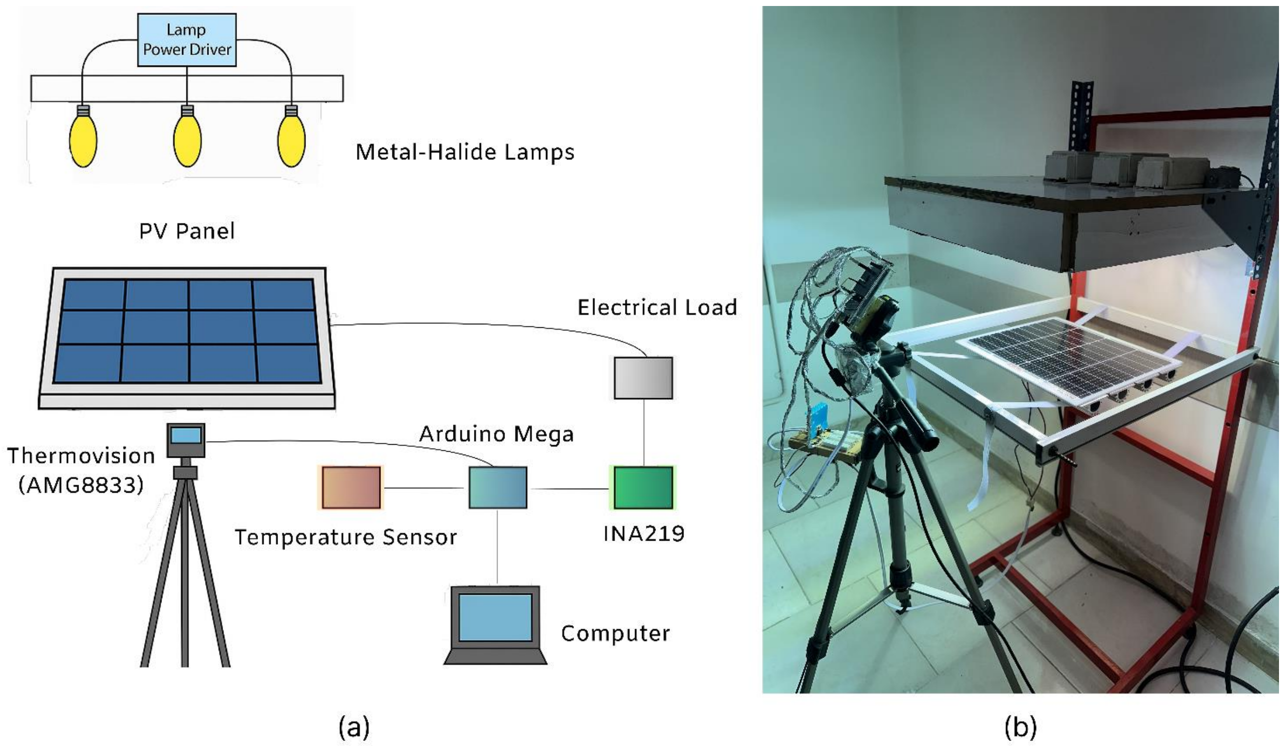

Figure 1. (a) Schematic representation of the experimental setup. (b) Photograph of the PV panel with attached heat sink (Model A).

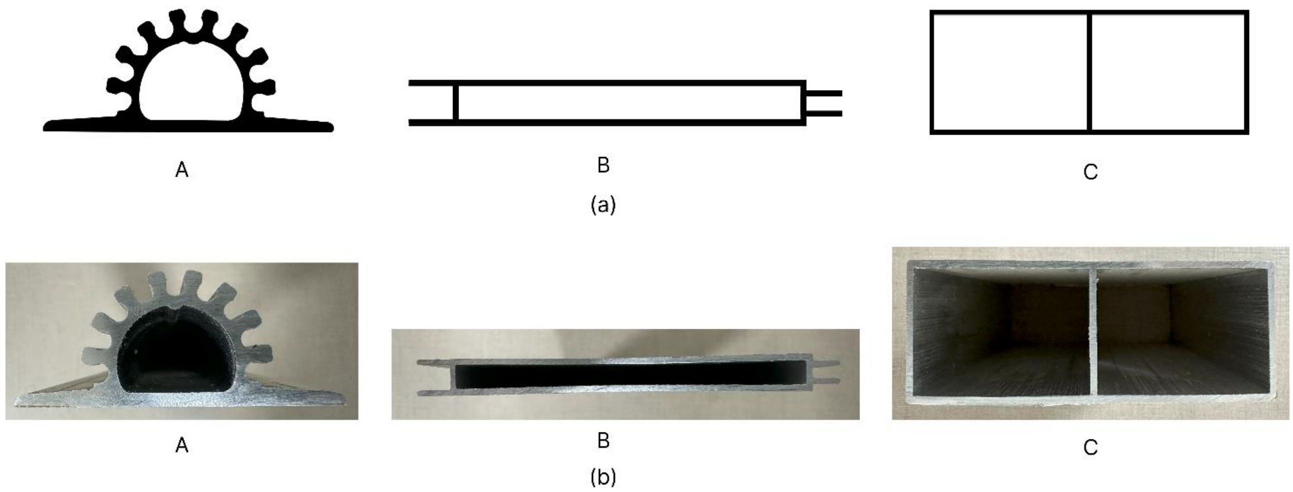

Figure 2. (a) schematic of the heat sinks. (b) Photograph of the heat sinks.

Table 1. Key specifications of the monocrystalline PV panel.

Feature	Value
Brand/Model	NN-M36-20W
Maximum Power (Pm)	20 (W)
Voltage at Maximum Power (Vmp)	20.84 (V)
Current at Maximum Power (Imp)	1.44 (A)
Open-Circuit Voltage (Voc)	24.8 (V)
Short-Circuit Current (Isc)	1.53 (A)
Maximum System Voltage	1000 (V)
Operating Temperature	-40 to +85 (℃)
Technology	Monocrystalline Silicon
Dimensions	330×400×17 (mm)
Weight	1.38 (Kg)
Power Tolerance	0 to +3 (W)
Temperature Coefficient	-0.45 %/°C

Table 2. Geometric, physical specifications and price of the aluminum heat sink models.

Model	Total Mass (g)	Price ($)	Effective contact Area with panel (%)	Number of Rows	Width per Row (mm)
A	2168	≈8.7	89.8	4	73
B	900	≈3.6	100	4	82.5
C	1440	≈5.8	98.4	4	80

Effective contact area (%) indicates the percentage of the heat sink base directly bonded to the PV rear surface via silicone adhesive, affecting initial heat transfer efficiency.

2.2. Sensors and data acquisition system

In this experimental work, the Arduino Mega 2560 microcontroller was selected for real-time monitoring due to its robustness and compatibility with multiple sensors. Data were sampled at 10 Hz and averaged every 30 seconds to mitigate noise and capture dynamic responses. Processed data were transferred via USB to a Python script for logging.

- Surface Temperature: An AMG8833 infrared array sensor (Panasonic) provided distributed temperature mapping via an 8×8 pixel array (software-interpolated to 256×256), connected via I²C protocol. Utilizing this sensor enabled the detection of thermal gradients across the panel.
- Ambient Temperature: A DS18B20 digital sensor (Maxim Integrated) using One-Wire communication was positioned in a shaded location to accurately measure ambient temperature.
- Electrical Parameters: An INA219 module (Texas Instruments) measured voltage, current, and power output directly in the circuit, interfaced via I²C.

2.3. Calibration Procedures

Sensors were calibrated via software-based corrections applied in the Arduino code prior to each experimental run, using reference standards to enhance accuracy.

- AMG8833: This sensor was calibrated across the 25–80°C range against a certified reference thermometer, with offsets applied to achieve an accuracy of ±0.5°C.
- DS18B20: This digital temperature sensor was tested in a regulated-temperature water bath against a certified reference thermometer, with corrections resulting in ±0.3°C precision.
- Ina219: This sensor was validated with a calibrated multimeter across its operational ranges (0–30 V, 0–2 A), with scaling factors applied to reduce errors to less than 1%.

2.4. Uncertainty analysis

The reliability of the obtained data was quantified by means of error propagation analysis. For a dependent variable R=f (x_1, x_2, …, x_n), Combined uncertainty was computed via root-sum-square (RSS) error propagation [25]:

$$\delta R = \sqrt{\left(\frac{\partial f}{\partial x_1}\delta x_1\right)^2 + \left(\frac{\partial f}{\partial x_2}\delta x_2\right)^2 + \cdots + \left(\frac{\partial f}{\delta \partial_n}\delta x_n\right)^2} \qquad (1)$$

The relative uncertainties for multiplicative parameters, such as power (P = VI), were calculated as follows:×

$$\frac{\delta P}{P} = \sqrt{\left(\frac{\delta V}{V}\right)^2 + \left(\frac{\delta I}{I}\right)^2} \qquad (2)$$

Type A (repeatability from temporal variability in the time series) and Type B (instrumental) components were combined, with expanded uncertainty at 95% confidence (k = 2). Table 3 lists key values for critical metrics, where the relative error was minimized to less than 5% through calibration and averaging. Uncertainty propagation was applied to derived quantities, such as heating rates and power output, using the RSS method. For example, the heating rate (ΔT/Δt) incorporates uncertainties from panel surface temperature (±0.5°C, combined Type A and B) and time measurement (negligible, <0.1 s). This results in a propagated uncertainty of approximately ±0.05°C/min for rates in the 0–30 min interval, ensuring that comparisons between configurations remain statistically significant. Expanded uncertainties (k = 2, 95% confidence) were calculated for all key metrics, minimizing relative errors to less than 5% through data averaging and calibration, as detailed in table 3.

Table 3. Uncertainties for primary measurements.

Measurement	Accuracy	Uncertainty Type
Ambient Temperature	±0.5 ℃	B
Solar Irradiance	±3%	B
Panel Surface Temperature	±0.5 ℃	Combined (A&B)
Power	±1.4%	Combined (A&B)
Mass	±1g	B

Repeatability inferred from reference runs and low SD (<1.4%), inter-trial stats in future work.

2.5. Experimental protocol

The tests were conducted in a closed environment without wind (forced convection), following these steps: (1) assembly of the PV panel with the selected heat sink geometry; (2) stabilization period for thermal equilibrium (6 hours); (3) activation of the solar simulator with a 5-minute warm-up (the panel was shielded); (4) each scenario (the reference case and all heat sink models) underwent 60 minutes of data collection.

A maximum power point tracking (MPPT) algorithm on the Arduino was applied to control load resistance via PWM and a MOSFET (IRL3103) to maintain optimal operation. Safety protocols included electrical insulation and thermal safeguards. High-resolution images of all configurations were archived for reproducibility and future reference. This protocol enabled a systematic comparison of the effects of heat sink geometries on temperature and power, with all conditions (e.g., irradiance, ambient temperature) held constant.

2.6. Theoretical background

The energy balance for a PV module can be expressed as:

$$Q_{solar}=Q_{electrical}+Q_{conv}+Q_{rad}+Q_{cond} \quad (3)$$

where Q_{solar}=G×A, $Q_{electrical}$=η×G×A, and the remaining terms correspond to convective, radiative, and conductive heat dissipation. The convective coefficient h_c under natural convection can be estimated as:

$$h_c=C(\Delta T/L)^n \quad (4)$$

depending on geometric and environmental parameters [17, 21]. The inclusion of an aluminum heat sink enhances A_{eff} and the conductive path, thereby reducing T_p. These relations underpin the physical interpretation of measured temperature and power variations in subsequent sections. Substituting these terms yields the instantaneous thermal balance as $(1-\eta)G\,A = h_c\,A_{eff}(T_s - T_a) + \varepsilon\sigma A_{eff}(T_s^4 - T_{sky}^4)$, demonstrating that any increment in A_{eff}or $h_c$reduces the surface temperature $T_s$and enhances conversion efficiency. This framework provides the theoretical justification for the trends observed in Section 3 (ΔT and efficiency variations among models A–C).

3. Results and discussion

This section presents the experimental findings on how various aluminum heat sink designs influence temperature reduction and enhance power output in photovoltaic (PV) panels under steady artificial light. The experimental data were obtained by evaluating three heat sink designs (Models A, B, and C) against a reference setup (non-cooled panel) under controlled laboratory conditions. Tests were conducted under fixed conditions—specifically, an irradiance of approximately 1000 W/m² ± 3% and an ambient temperature maintained between 25–27°C—to isolate the effects of heat sink geometry.

Surface temperature (averages and peaks), temperature change rates, and power output were tracked. To suppress noise, we applied a five-point simple moving average (SMA) to the data. timeline segmented as follows: 0–30 minutes for the initial heating phase, 30–60 minutes for the stabilization period approaching steady state.

Results are presented in figures 3–8 and tables 4 and 5, accompanied by interpretations, discussion of practical implications, study limitations, and suggestions for future research. All data were obtained from repeatable experimental runs. Measurement uncertainties, as quantified in table 3 of the Methods section, were incorporated into the analysis to ensure robustness.

3.1. Temperature distribution and thermal stability

Surface temperatures of the PV panel, measured using the AMG8833 infrared sensor, were the primary metric for thermal performance evaluation. Raw data revealed a sharp increase early on, followed by a slowdown toward stability. Figure 3 displays the temporal progression of the panel surface temperature. Figure 4 illustrates the smoothed temperature profile.

To validate the data smoothing process, temperature residuals were calculated as the differences between raw temperature measurements and smoothed temperature. Figure 5 presents temperature residuals over time. The residuals for all configurations exhibit random fluctuations primarily within ±2°C (with occasional peaks up to +5°C in the first 10 minutes). Notably, the residuals oscillate around zero without defined trends, indicating that the SMA effectively filtered out high-frequency noise while preserving the underlying thermal dynamics, thereby validating the appropriateness of the smoothing technique and enhancing the reliability of subsequent analyses, such as heating rate calculations in table 4.

Over the first 30 minutes, the temperature increase was greatest for the reference case (33.73°C), followed by Model B (32.61°C), with Model A showing the least rise (31.17°C) due to its superior thermal inertia. The use of other heat sinks mitigated this effect, lowering the rise to 31.61°C for heat sink Model A and 33.39°C for Model C. With a rate of 1.331°C/min, the reference case heated faster than the cooled setups. Heat sinks are more effective due to their dual functionality; they efficiently dissipate heat away from concentrated hot spots and serve as a temporary thermal buffer. This synergistic effect reduces the rate of temperature increase. This finding is supported by the thermal imagery taken at 30 minutes (Figure 6), which visually demonstrates the attenuated thermal gradients present in the actively cooled configurations.

As the temperature approached its steady state, its rate of increase noticeably slowed, indicating the system was reaching thermal equilibrium. The extra mass of the heat sinks causes a thermal delay: they first absorb heat and require time to balance and release it. The 60-minute thermal images (Figure 7) confirm this, clearly showing that Model B distributes heat more evenly than the others. During the 30–60 minutes period, the heating rate decreased (0.09–0.22°C/min), and the heat sink configurations (A: 6.72°C, B: 3.04°C, C: 4.13°C) demonstrated a greater overall temperature increase than the reference panel (2.59°C). Temperature values and rates are presented in table 4.

For this study, we defined thermal stability as maintaining a heating rate below 0.1°C/min for a period of 30 minutes; the reference case achieved this stability during the 30–60 minutes interval. The use of a heat sink delayed the time to reach thermal stability. Specifically, propagated uncertainties from table 3 (e.g., ±0.5°C for surface temperature) were incorporated into heating rate calculations (Table 4), yielding confidence intervals of ±0.04–0.07°C/min for the reference case (1.331°C/min in 0–30 min). This confirms that observed differences (e.g., Model A reducing initial heating by approximately 6% compared to the reference) are reliable, with relative errors less than 5%, thereby increasing confidence in the heat sinks' thermal buffering efficacy.

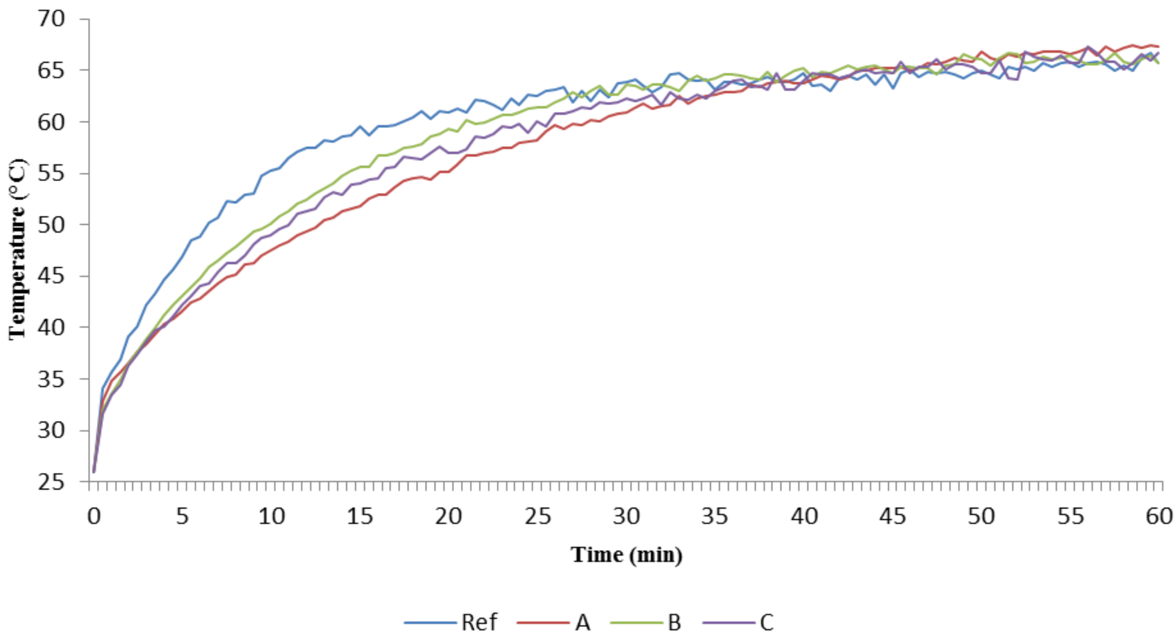

Figure 3. Raw average panel surface temperatures over time for each setup.

Figure 3 shows the raw average surface temperatures of the PV panel over 60 minutes for the reference (Ref) and heat sink models (A, B, C). The reference exhibits the fastest initial rise (reaching ~63°C by 30 min), while models A, B, and C show delayed heating due to thermal buffering, with model A performing best in mitigating early temperature spikes. High-frequency noise is evident, particularly in the first 30 minutes, reflecting sensor variability under constant irradiance (~1000 W/m²).

Figure 4 presents the smoothed average surface temperatures after applying a 5-point simple moving average (SMA), revealing clearer monotonic trends toward steady-state. The reference reaches equilibrium fastest (~0.1°C/min heating rate after 30 min), whereas heat sink models delay stabilization (e.g., model B shows the slowest rise in 30–60 min, with a total increase of 3.04°C), highlighting their role in attenuating thermal gradients and supporting the observed heating rates in table 4.

Figure 5 illustrates the residuals (differences between raw and smoothed temperatures), oscillating randomly around zero within ±2°C (with peaks up to +5°C in the first 10 min) across all configurations. The absence of systematic trends validates the SMA smoothing efficacy in filtering noise without biasing underlying dynamics, ensuring reliable derivation of heating rates (e.g., reference at 1.331°C/min in 0–30 min) and uncertainty estimates (<5% relative error).

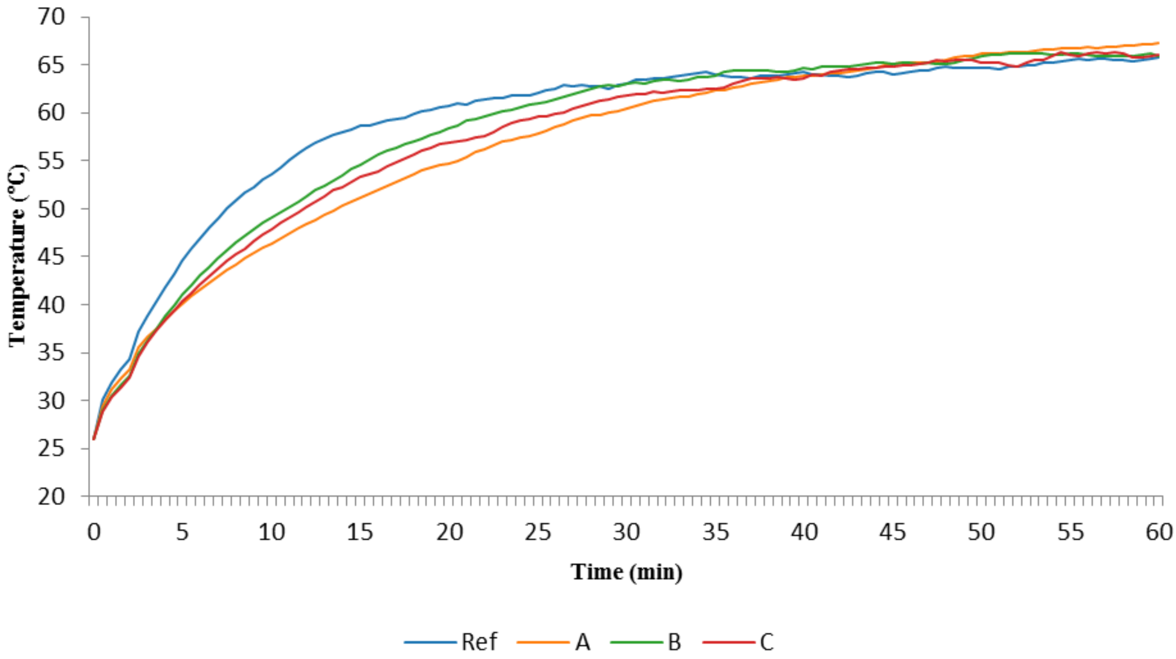

Figure 4. Smoothed panel surface temperatures over time.

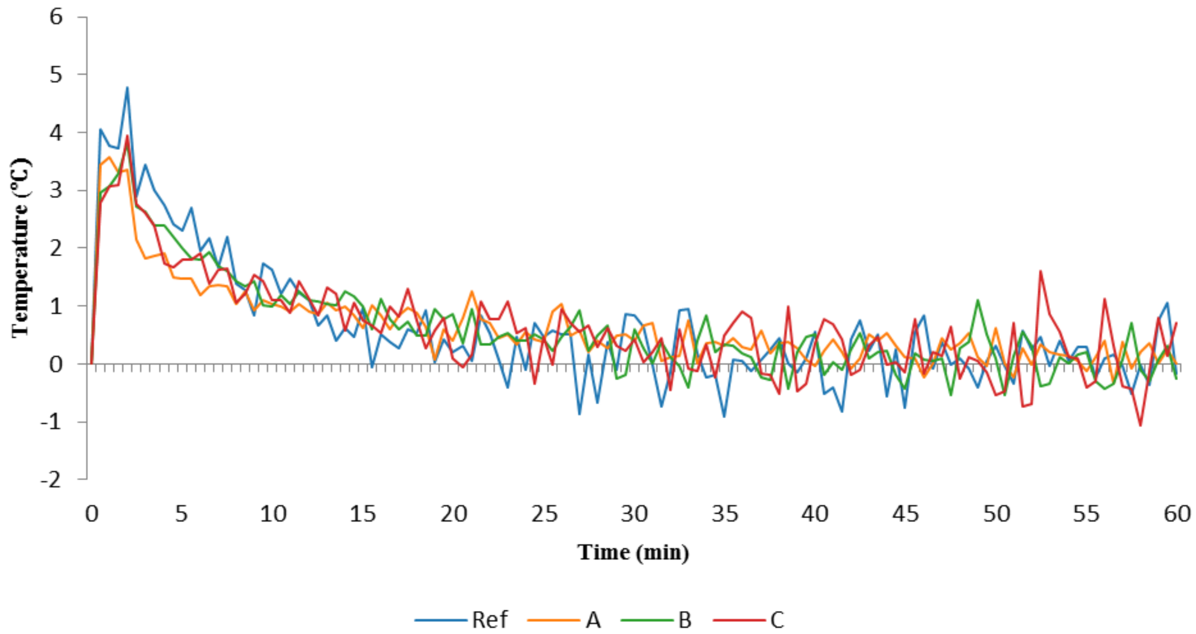

Figure 5. Temperature residuals over time.

Table 4. Temperature values and rates.

Model	Temperature At 30 min (℃)	ΔTemperature from Ref At 30 min (℃)	Heating rate 0-30 min (℃/min)	Temperature At 60 min (℃)	ΔTemperature from Ref At 60 min (℃)	Heating rate 30-60 min (℃/min)	Heating rate 0-60 min (℃/min)
Ref	63.06	–	1.23	65.66	–	0.08	0.66
A	60.50	−2.56	1.15	67.23	+1.57	0.22	0.68
B	62.99	−0.07	1.23	66.04	+0.38	0.10	0.66
C	61.77	−1.29	1.19	65.91	+0.25	0.13	0.66

Note: Uncertainties (k=2) from table 3; SD ≈ ±0.5°C

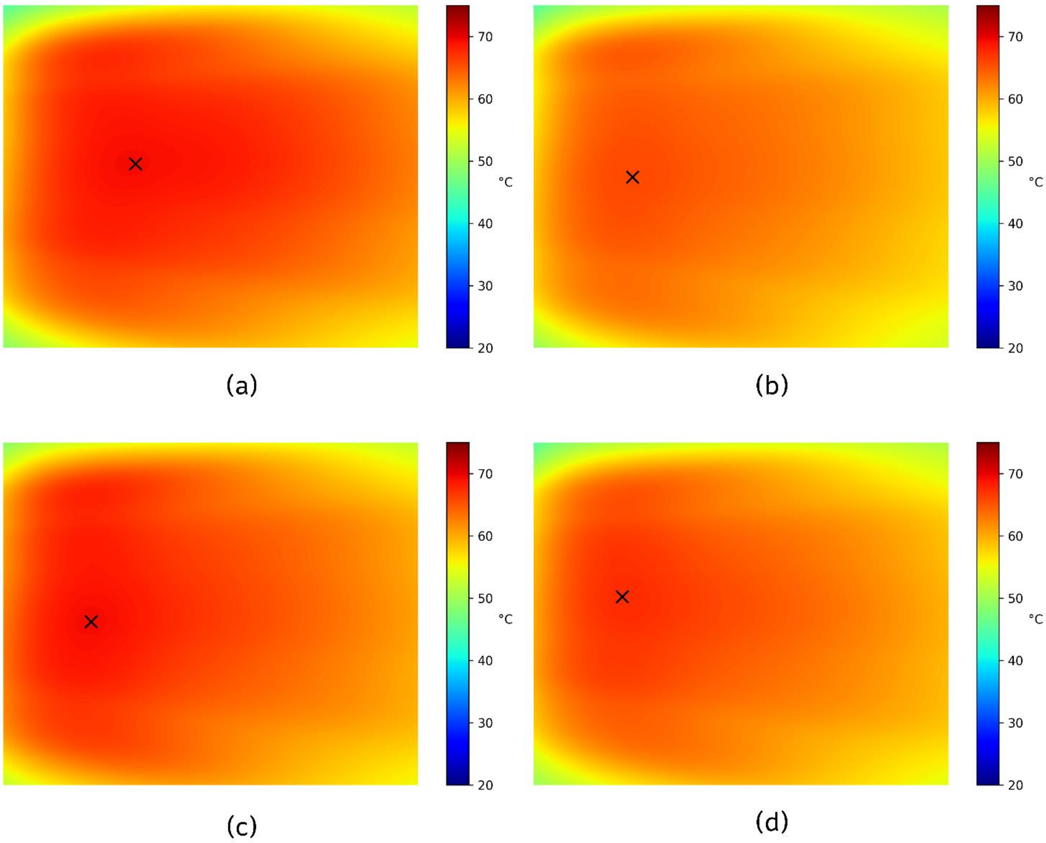

Figure 6. Thermal images of the panel at 30 minutes. (a) Ref. (b) Model A. (c) Model B. (d) Model C.

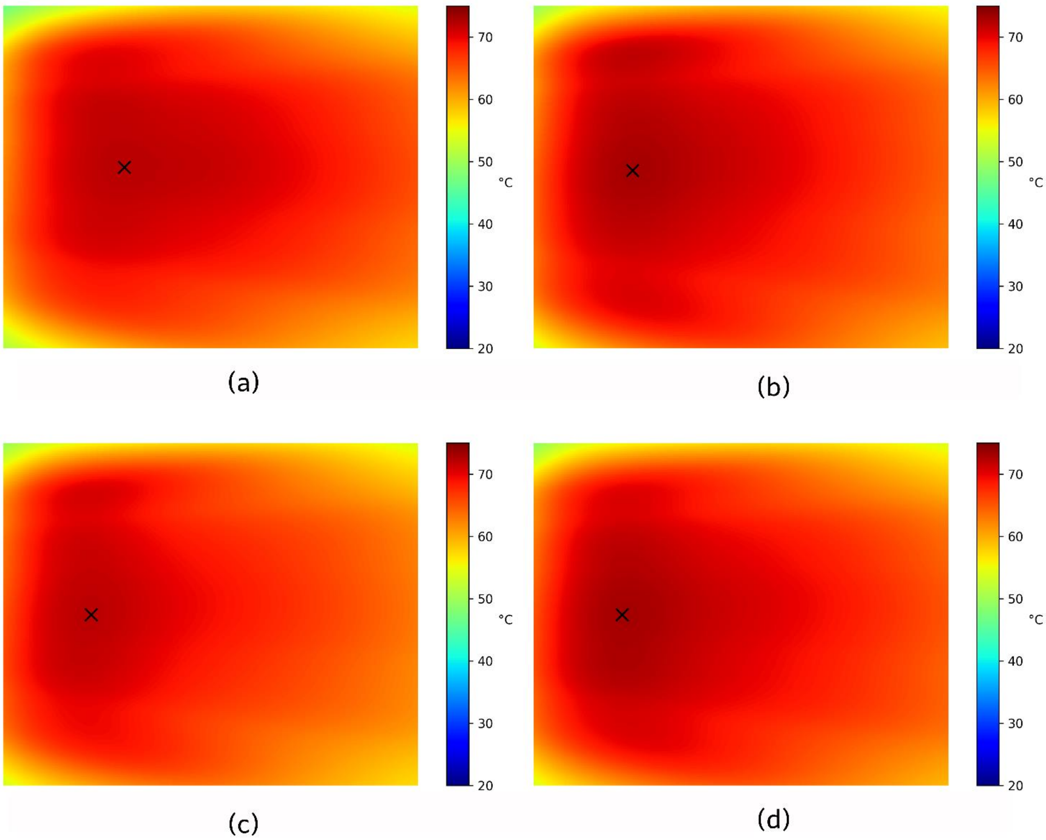

Figure 7. Thermal images of the panel at 60 minutes. (a) Ref. (b) Model A. (c) Model B. (d) Model C.

Non-uniformity (higher temperatures on the left side, ΔT ≈ 2–3°C) was observed across all cases, including the reference. This pattern originated from the combined effect of the IR sensor's angled view/interpolation and a slight (~3%) irradiance asymmetry among solar-simulator lamps. The heat sink installation (4 rows, centered) minimizes but does not eliminate this; it does not influence averaged thermal or power outcomes (Table 4).

The temperatures in table 4 are the average panel surface temperatures obtained by averaging the measured temperatures from the panel surface at each time, using the AMG8833 module.

3.2. Electrical output and performance

Power output was measured using the INA219 module and smoothed with a 5-point Simple Moving Average (SMA) to reduce fluctuations. Figure 8 presents the smoothed power output trends from 0 to 60 minutes and indicates a downward trend in power output. The experiment began with the panel producing approximately 23 watts of power in all scenarios. In the first 30 minutes, power output decreased sharply, with power dropping to around 21–22 W across models. At 30 minutes, power output measurements revealed the following values: the uncooled reference panel at 21.17 ± 0.30 W, Model A at 21.52 ± 0.30 W, Model B at 20.86 ± 0.29 W, and Model C at 21.25 ± 0.30 W.

Final power measurements at 60 minutes showed a slight decrease for all cooled models relative to the uncooled reference (20.89 ± 0.29 W): Model A at 20.63 W (−1.24%), Model B at 20.73 W (−0.77%), and Model C at 20.75 W (−0.67%); all uncertainties ±0.29 W.

These power output trends directly correspond to the observed temperature profiles. Raw data residuals and uncertainty propagation confirm data reliability, providing a robust basis for subsequent analyses.

Our results align with the established thermal dependence of photovoltaic cells, where elevated temperatures accelerate efficiency losses. Table 5 presents detailed power values, absolute differences (ΔP), and percentage changes (%ΔP) relative to the PV reference at 30 and 60 minutes.

From experimental data, the practical temperature coefficient was derived as $\beta = \frac{\Delta P/P}{\Delta\theta} \approx -0.42\ \frac{\%}{°C}$, closely matching the manufacturer's nominal $-0.45\ \frac{\%}{°C}$ (Table 1).

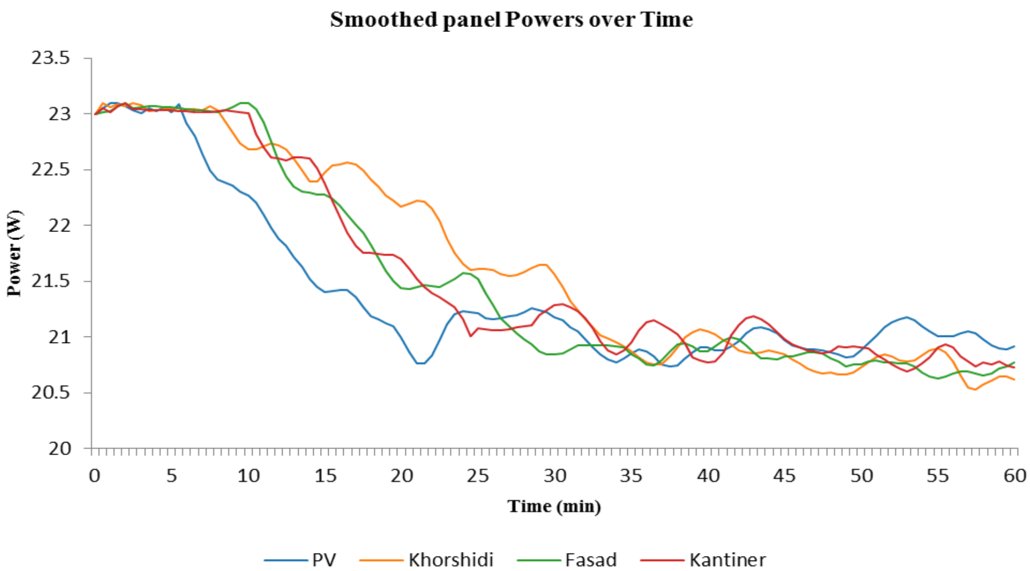

Figure 8. Smoothed panel output powers over time.

Table 5. Power Values, Differences, and Percentage Changes.

Model	Power at 30 min (W)	ΔPower from Ref at 30 min (W)	% Change from Ref at 30 min	Power at 60 min (W)	ΔPower from Ref at 60 min (W)	% Change from Ref at 60 min
Ref	21.17	–	–	20.89	–	–
A	21.52	+0.35	+1.65%	20.63	−0.26	−1.24%
B	20.86	−0.31	−0.31%	20.73	−0.16	−0.77%
C	21.25	+0.08	+0.37	20.75	−0.14	−0.67%

Note: Uncertainties (k=2) from table 3; SD ≈ ±1.4%

3.3. Discussion

The results from this study highlight that aluminum heat sink geometries can influence the thermal and electrical performance of PV panels under controlled irradiation, although the effects are nuanced and depend on time. Specifically, the observed temperature profiles and power outputs underscore the role of heat sink mass in influencing heat dissipation through natural convection and radiation. In the initial heating phase (0-30 minutes), all heat sink models (A, B, and C) effectively reduced the rate of temperature rise compared to the reference case, with Model A demonstrating the most significant mitigation ($\Delta T = -2.56°C$ at 30 minutes). This aligns with and confirms the role of heat sinks as thermal buffers; they absorb excess heat and distribute it over a larger surface area, thus reducing temperature increase, as shown in the thermal images (Figure 5). However, during the stabilization phase (30-60 minutes), the cooled models showed higher overall temperature increases (e.g., Model A: +1.57°C relative to the reference at 60 minutes), leading to slightly lower power outputs (e.g., -1.24% for Model A). This counterintuitive outcome can be attributed to the heat sink's geometry. A suboptimal heat sink geometry can alter airflow patterns, leading to hot air entrapment and redirecting heat back toward the heat sink rather than allowing efficient dissipation. Consequently, the PV cells experienced sustained elevated temperatures, exacerbating efficiency losses due to the negative temperature coefficient of silicon-based modules (typically -0.4% to -0.5% per °C above 25°C).

These findings are consistent with prior studies on passive cooling for PV systems. Our delayed stabilization with heavier designs parallels studies linking increased mass to extended transient phases in natural convection scenarios [26]. In a similar vein, the initial temperature mitigations we observed align with work on finned aluminum profiles, which demonstrated short-term reductions but warned of inefficiencies without external airflow [2]. We also noted modest power gains under stagnant conditions, echoing findings that reported under 2% improvements for passive setups, far below forced-convection outcomes [5]. Finally, the eventual power dips in our tests mirror radiative heat entrapment effects highlighted in prior thermal modeling, emphasizing limitations in unventilated environments [21]. The slight power reduction after reaching thermal stability showed that, despite the benefits of greater heatsink mass in short-term exposures and the delay in the initial temperature rise, it caused temperature increases over longer periods.

The practical significance of these results is underscored in regions like Iran, which experiences both extreme heat and high solar insolation, where high ambient temperatures and abundant solar resources necessitate cost-effective cooling solutions. The use of locally available industrial aluminum profiles (as in this study) offers a low-cost (≈4$/kg) alternative to active cooling systems. Economically, integrating such heat sinks could enhance annual energy yield in utility-scale installations, based on temperature reductions, though full lifecycle assessments are needed to quantify payback periods.

Despite these contributions, it is important to acknowledge the study's limitations. The experiments were limited to a 60-minute duration in a wind-free indoor environment and do not emulate real operational conditions (e.g., fluctuating solar irradiance, wind-driven convection, and dust accumulation). Although investigating only three readily available, cost-driven heatsink geometries may have overlooked designs with superior thermal characteristics (e.g., higher fin density), future research should involve longer test durations and computational fluid dynamics (CFD) modeling to predict optimal geometries. Outdoor large-scale experiments, incorporating forced convection, varying wind speeds, and hybrid methods (such as phase-change material integration), are essential for validation. Additionally, future studies should include a comparative assessment with commercial finned heat sinks to provide benchmark performance data under identical boundary conditions. Ultimately, technical and economic analyses coupled with pilot deployments in operational solar farms will be crucial for transitioning this laboratory research into practical, high-efficiency photovoltaic technology.

4. Conclusion

This experimental study assessed the effects of three distinct aluminum heat sink geometries (Models A, B, and C) on the thermal and electrical performance of a monocrystalline silicon photovoltaic (PV) panel under controlled irradiation conditions simulating approximately 1000 W/m² ± 3% with zero wind speed, focusing on natural convection. The findings reveal subtle and time-dependent impacts: during 0–30 minutes (the initial heating phase), all heat sink models effectively mitigated temperature rises compared to the uncooled reference case, with Model A achieving the most significant temperature decrease (ΔT = -2.56°C at 30 minutes) and power increase (up to +1.65%). However, in 30–60 minutes (the stabilization phase), the heat sinks led to increased temperature (e.g., +1.57°C for Model A at 60 minutes) and modest power reductions (-0.67% to -1.24%) relative to the reference. These findings highlight the dual role of heat sinks as thermal buffers that absorb and dissipate heat initially but may trap hot air due to suboptimal geometries, leading to efficiency losses in PV modules with negative temperature coefficients. The significance of these findings lies in their demonstration that heat sink mass and design critically influence short-term versus long-term performance, highlighting the limitations of passive cooling under low-airflow conditions while quantifying modest efficiency improvements that could enhance energy yield in controlled environments.

In the initial heating phase, the superior performance of Model A stems from its higher mass (2168 g; Table 2), which acts as an effective thermal buffer despite a slightly reduced effective contact area with the panel (89.8%), absorbing excess heat and delaying the rise rate to 1.15°C/min (vs. 1.23°C/min for Ref; Figure 4). This contact area—representing the percentage of the heat sink base in direct thermal contact with the PV rear surface via silicone adhesive—facilitates initial heat transfer, though its partial coverage in Model A is offset by mass-driven inertia. Models B and C provided moderate benefits (ΔT = -0.07°C and -1.29°C at 30 minutes; Table 4), leveraging fuller contact areas (100% and 98.4%) for enhanced heat extraction from the panel, yet their lower masses (900 g and 1440 g) result in diminished buffering. Thermal images (Figure 6) at 30 minutes further illustrate attenuated temperature gradients across the panel surface in cooled configurations, underscoring how geometry influences early convection and radiation efficiency under stagnant conditions.

During the stabilization phase, the observed temperature upticks and power losses (e.g., -1.24% for Model A; Table 5) arise from geometry-induced hot air entrapment, where denser fin channels in heavier models like A prolong heat retention (stabilization rate 0.22°C/min vs. 0.08°C/min for Ref; Figure 7). The partial contact area in Model A exacerbates this by allowing uneven heat redistribution, redirecting warmth back to the PV cells and amplifying the silicon negative temperature coefficient effect (-0.45%/°C above 25°C). In contrast, lighter Model B stabilizes more rapidly (0.10°C/min; +0.38°C relative), benefiting from full contact for efficient initial transfer and minimal mass to avoid prolonged retention, while Model C's intermediate design offers a balanced outcome (+0.25°C). These trade-offs—high contact area enabling optimal short-term transfer (Models B/C) versus mass providing sustained buffering (Model A)—reveal natural convection's constraints, with overall net gains under 2% and measurement uncertainties below 5% (Table 3) confirming result robustness. Such insights position heavier profiles like Model A as viable low-cost (~4$/kg) options for transient hot-arid applications, such as in wind-free regions of Iran. Overall, these findings directly address the original research objective—to evaluate the baseline cooling capability of industrial aluminum profiles under stagnant-air conditions. The observed temperature moderation and corresponding power variations confirm that commercial channel profiles can provide short-term buffering benefits, yet emphasize the intrinsic limitations of purely passive natural convection. Consequently, the study establishes a quantitative reference for subsequent development of hybrid or geometry-optimized designs, bridging experimental observations with the practical need for cost-effective PV thermal management in arid climates. Future enhancements could repurpose the channel voids for PCM encapsulation (e.g., paraffin-based materials), mitigating stagnation effects observed here and enabling direct comparisons with unmodified profiles for optimized PV thermal management. Future work should incorporate 3–5 repetitions per model to compute standard deviation (SD) metrics, further validating the time-dependent trends and enhancing reproducibility in natural convection assessments.

5. Nomenclature

Symbol	Description	Unit
A	Effective contact area between heat sink and PV panel	%
A_{eff}	Effective external area for convective and radiative heat dissipation	m^2
β	Temperature coefficient of power	% / °C
ε	emissivity	–
σ	Stefan's constant	$W/m^2.K^4$
G	Solar irradiance	W / m^2
h_c	Convective heat-transfer coefficient	$W / m^2 \cdot K$
I, I_{mp}, I_{sc}	Current / at maximum power /	A

	short-circuit current	
k	Coverage factor for expanded uncertainty (95 % conf., k = 2)	–
L	Characteristic length (e.g., fin height or channel spacing)	m
m	Mass	g
n	Empirical exponent in convective correlation	–
n_{rows}	Number of fin rows in sink geometry	–
P, P_m	Electrical power / maximum power	W
Q_{solar}, $Q_{electrical}$, Q_{conv}, Q_{rad}, Q_{cond}	Solar input, electrical output, convective, radiative and conductive heat components	W
RH	Relative humidity	%
t	Time	Min
T, T_a, T_p, T_{sky}, ΔT	Surface / ambient / peak / sky / temperature difference	°C
ΔT/Δt	Heating rate	°C / min
V, V_{mp}, V_{oc}	Voltage parameters	V
w	Width per fin row	Mm
η	Electrical conversion efficiency	%
δV/V, δI/I, δ P/P, δG/G, δT, δm	Measurement uncertainties	%, °C, g
PCM	Phase change material	–
RH	Relative humidity	%
SMA	Simple moving average	–
RSS	Root sum square	–

6. References

[1] A. M. Bukar, A. Almerbati, S. Z. Shuja, and S. M. Zubair, “Enhancing solar PV panel performance through active and passive cooling techniques: A comprehensive review,” Renewable and Sustainable Energy Reviews, vol. 216, pp. 115611, 2025/07/01/, 2025.

[2] R. Salehi, A. Jahanbakhshi, J. B. Ooi, A. Rohani, and M. R. Golzarian, “Study on the performance of solar cells cooled with heatsink and nanofluid added with aluminum nanoparticle,” International Journal of Thermofluids, vol. 20, pp. 100445, 2023/11/01/, 2023.

[3] R. Chandel, S. S. Chandel, and A. Khosla, “Modelling and experimental investigation of cooling of field-operating PV panels using thermoelectric devices for enhanced power generation by industrial solar plants,” Next Energy, vol. 5, pp. 100162, 2024/10/01/, 2024.

[4] E. Chan-Dzib, J. G. Carrillo, A. Bassam, L. D. Patino Lopez, A. J. Cetina-Quiñones, and M. Flota-Bañuelos, “Hybrid thermal CFD-quadrupole simulation method for estimating the cooling performance of a PV panel under natural weather conditions,” International Journal of Thermal Sciences, vol. 210, pp. 109576, 2025/04/01/, 2025.

[5] M. S. Tahir, X. Dong, M. M. Khan, and I. U. Rehman, “Thermal management of photovoltaic systems: a comprehensive review of cooling strategies,” Solar Energy, vol. 299, pp. 113811, 2025/10/01/, 2025.

[6] I. O. Harmailil, S. M. Sultan, A. Fudholi, M. Mohammad, and C. P. Tso, “A new cooling method for photovoltaic module using U-shape aluminum fins and circular copper tubes: An indoor experiment and economic study,” Case Studies in Thermal Engineering, vol. 72, pp. 106396, 2025/08/01/, 2025.

[7] S. N. Razali, A. Ibrahim, A. Fazlizan, M. F. Fauzan, R. K. Ajeel, E. Zairah Ahmad, W. E. Ewe, and H. A. Kazem, “Performance enhancement of photovoltaic modules with passive cooling multidirectional tapered fin heat sinks (MTFHS),” Case Studies in Thermal Engineering, vol. 50, pp. 103400, 2023/10/01/, 2023.

[8] I. O. Harmailil, S. M. Sultan, C. P. Tso, A. Fudholi, M. Mohammad, and A. Ibrahim, “A review on recent photovoltaic module cooling techniques: Types and assessment methods,” Results in Engineering, vol. 22, pp. 102225, 2024/06/01/, 2024.

[9] H. A. Kazem, A. A. Al-Waeli, M. T. Chaichan, K. Sopian, A.-A. Ahmed, and W. I. Wan Nor Roslam, “Enhancement of photovoltaic module performance using passive cooling (Fins): A comprehensive review,” Case Studies in Thermal Engineering, vol. 49, pp. 103316, 2023/09/01/, 2023.

[10] Q. Peng, D. Li, X. Sun, J. Li, Y. Zhou, and L. Zeng, “Experimental and numerical investigation on photovoltaic/thermal characteristics of an integrated PV/T-PCM system with metal fin and heat exchange pipe,” Renewable Energy, vol. 239, pp. 122113, 2025/02/01/, 2025.

[11] M. E. Hadi Attia, A. Khelifa, A. E. Kabeel, M. Fayed, W. M. El-Maghlany, and N. A. Moharram, “A novel PVT system integrated with semicircular fins: CFD-based analysis of heat dissipation and energy efficiency,” Applied Thermal Engineering, vol. 279, pp. 127551, 2025/11/15/, 2025.

[12] D. Değirmenci, E. Çubuk, İ. Tarı, and Ö. Selimoğlu, “Cooling optimization for concentrating photovoltaic modules: A study of convective and radiative cooling with a focus on plate fin applications,” Renewable Energy, vol. 247, pp. 122953, 2025/07/01/, 2025.

[13] H. Abdulla, A. Sleptchenko, and A. Nayfeh, “Photovoltaic systems operation and maintenance: A review and future directions,” Renewable and Sustainable Energy Reviews, vol. 195, pp. 114342, 2024/05/01/, 2024.

[14] M. A. Akrouch, K. Chahine, J. Faraj, F. Hachem, C. Castelain, and M. Khaled, “Advancements in cooling techniques for enhanced efficiency of solar photovoltaic panels: A detailed comprehensive review and innovative classification,” Energy and Built Environment, vol. 6, no. 2, pp. 248–276, 2025/04/01/, 2025.

[15] A. M. Oni, A. S. M. Mohsin, M. M. Rahman, and M. B. Hossain Bhuian, “A comprehensive evaluation of solar cell technologies, associated loss mechanisms, and efficiency enhancement strategies for photovoltaic

cells," Energy Reports, vol. 11, pp. 3345–3366, 2024/06/01/, 2024.

[16] H. Luqman Azeez, A. Ibrahim, B. Omer Ahmed, A. H. A. Al-Waeli, M. Jaber, and M. Aqil Afham Rahmat, "Energy and exergy analysis of a novel collector design in a photovoltaic thermal system: An experimental study," Applied Thermal Engineering, vol. 256, pp. 124125, 2024/11/01/, 2024.

[17] H. A. Refaey, M. A. Alharthi, S. Bendoukha, S. G. Khan, M. Emam, and M. A. Abdelrahman, "An experimental investigation on passive cooling of a triple-junction solar cell at high concentrations using various straight-finned heat sink configurations," Case Studies in Thermal Engineering, vol. 51, pp. 103626, 2023/11/01/, 2023.

[18] H. B. Adedayo, K. Sopian, A. H. D. K. Rasangika, and O. I. Alonge, "Probing thermal dynamics in multi-layer solar photovoltaic modules: Unveiling hotspots and advancing innovative cooling strategies," Solar Energy, vol. 293, pp. 113470, 2025/06/01/, 2025.

[19] M. A. Tashkandi, A. Basem, H. A. Z. Al-bonsrulah, L. Kolsi, M. S. Albdeiri, L. Ben Said, and A. M. Hussin, "Numerical assessment of solar panel with utilizing ferrofluid flow within wavy duct equipped with V-shaped fins," Case Studies in Thermal Engineering, vol. 66, pp. 105800, 2025/02/01/, 2025.

[20] A. Ataman, and N. Arslanoğlu, "Investigation of the cooling effect of wind on rooftop PV power plants," Case Studies in Thermal Engineering, vol. 63, pp. 105295, 2024/11/01/, 2024.

[21] J. G. Hernandez-Perez, J. G. Carrillo, A. Bassam, M. Flota-Banuelos, and L. D. Patino-Lopez, "Thermal performance of a discontinuous finned heatsink profile for PV passive cooling," Applied Thermal Engineering, vol. 184, pp. 116238, 2021/02/05/, 2021.

[22] A. D. Tuncer, E. Y. Gürbüz, İ. Şahinkesen, A. Georgiev, and A. Keçebaş, "Passive cooling of photovoltaic panels with latent heat storage unit: Analyzing the effects of using fins and iron nanoparticles on the performance, economy and environmental impact," Energy, vol. 288, pp. 129860, 2024/02/01/, 2024.

[23] K. T. Alao, S. I. U. H. Gilani, K. Sopian, T. O. Alao, and Z. Aslam, "A comprehensive review of radiative cooling technologies and their integration with Photovoltaic (PV) systems: Challenges, opportunities, and future directions," Solar Energy, vol. 292, pp. 113445, 2025/05/15/, 2025.

[24] L. Lou, Z. Kang, H. Zhang, P. Wang, and J. Fan, "Nano-capillary aluminum finned heat sink for ultra-efficient evaporative cooling," Materials Today Physics, vol. 36, pp. 101175, 2023/08/01/, 2023.

[25] A. A. Jasim, A. Fazlizan, H. L. Azeez, A. Ibrahim, R. Almaawi, and K. Sopian, "Enhancing PV module performance through a novel fin heat sink design: A numerical and experimental study," Case Studies in Thermal Engineering, vol. 74, pp. 106842, 2025/10/01/, 2025.

[26] Z. Zhou, A. Gentle, M. Mohsenzadeh, Y. Jiang, M. Keevers, and M. Green, "Long-term outdoor testing of vortex generators for passive PV module cooling," Solar Energy, vol. 275, pp. 112610, 2024/06/01/, 2024.